Review

Inclusion Formation and Microstructure Evolution in Low Alloy Steel Welds

S. S. BABU and S. A. DAVID

Metals and Ceramics Division, Oak Ridge National Laboratory, Oak Ridge, TN 37831 USA. E-mail: babuss@ornl.gov

The paper presents an overview of research performed at Oak Ridge National Laboratory on inclusion-formation, weld-solidification, and solid–state transformations in low-alloy steel welds. The competition between oxide and nitride formation in Fe–C–Al–Mn self-shielded flux-cored arc steel welds was predicted using computational thermodynamics. Nonequilibrium austenite phase selection was monitored in a Fe–C–Al–Mn weld using an *in situ* time-resolved X-ray diffraction technique. The competition between acicular ferrite and bainite formation from austenite was evaluated in Fe–C–Mn steel welds containing small amounts of titanium.

KEY WORDS: steel welds; inclusion formation; weld solidification; nonequilibrium phase transformations; bainite; acicular ferrite.

1. Introduction

Creation of advanced structural steels and other alloys is achieved by reducing ferrite grain size through mechanical alloying, intensive plastic deformation, and or low-temperature phase transformations.[1-5] However, fusion welding with remelting and resolidification of these steels is expected to destroy the optimum microstructure that is obtained before welding. Therefore, new methods must be developed and conventional technology must be optimized to produce fine ferrite grain size in the weld metal. To achieve this goal, one must understand and control various physical processes that occur during welding of steels. **Figure 1** illustrates reaction sequences that occur in a low-alloy steel weld metal region.[6] At temperatures greater than 1 800 K, the dissolved gases react with alloying elements to form oxide or nitride inclusions. As the weld metal cools, the primary solidification occurs by the formation of the δ-ferrite phase through epitaxial growth of grains from the heat-affected-zone (HAZ). As the weld cools further, austenite may form in the interdendritic region and grow into the ferrite. Further cooling, below 1 600 K, leads to complete transformation of δ-ferrite to the austenite phase. With a decrease in temperature to ~1 000 K, allotriomorphic α-ferrite nucleates along the austenite grain boundaries. With a further drop in temperature, the allotriomorphic ferrite grows inward toward the center of the grain. Continued decrease in temperature leads to the formation of Widmanstatten ferrite followed by acicular ferrite and martensite.

In the past, extensive research has been done to relate the inclusion formation and decomposition of austenite in low-alloy steel welds.[7-26] Based on these research, it is possible to design welding consumables that maximize the forma-

tion of acicular ferrite in welds and thereby obtain better strength and toughness. However, the extension of this knowledge to a wide variety of welding processes, consumable compositions, and shielding gases still eludes welding metallurgist due to the complex interactions between inclu-
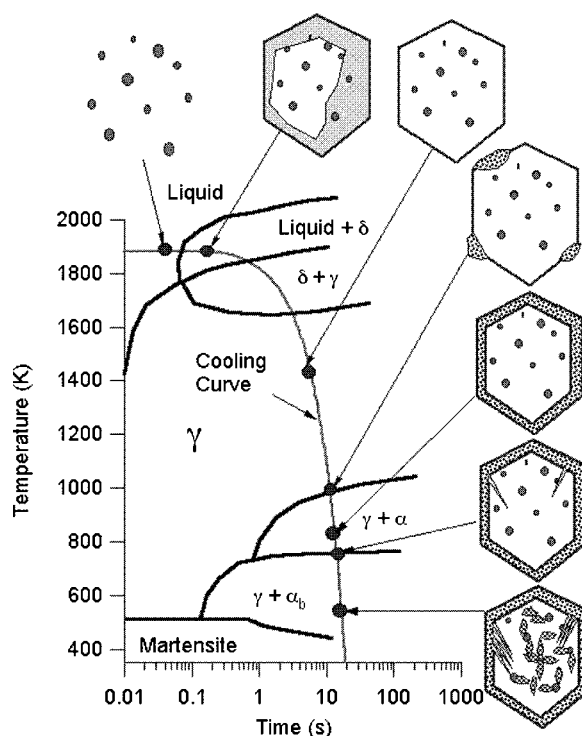
Fig. 1. Schematic illustration of inclusion formation; solidification to δ-ferrite; transformation of δ-ferrite to austenite; and decomposition of austenite to different α-ferrite morphologies, including allotriomorphic ferrite, Widmanstätten ferrite, bainite, and acicular ferrite.

sion formation, solidification, and solid-state transformations. The present overview focuses on current research activities at Oak Ridge National Laboratory (ORNL) that attempt to describe these interactions through computational thermodynamic and kinetic models, post-weld and in situ weld characterization.

2. Inclusion Formation

The first reaction that is known to influence the weld microstructure is inclusion formation.[27] Reactions between dissolved elements such as carbon, nitrogen, oxygen, aluminum, titanium, silicon, and manganese form the inclusions. The following inclusion characteristics affect the microstructure evolution: number density, volume fraction, composition, and heterogeneity of inclusions (surface and bulk composition). Previous research focused on developing thermodynamic and kinetic models to describe the inclusion characteristics as a function of weld metal composition and process parameters.[28] The model was based on sequential oxidation framework that was proposed originally by Bailey and Pargeter and by other researchers[29–32] and was later modified to include overall transformation kinetic theory.[33] This model removed the limitation of the fixed oxidation sequence assumed by other researchers and linked the oxidation sequence to the weld composition and cooling rate. This allowed the model to be applicable over wide range of weld compositions and the weld cooling rates. The model has been evaluated for both normal weld-cooling conditions as well as rapid cooling conditions typical of high-energy-density welding processes.[34]

Recently, the model has been coupled to numerical-heat-transfer and fluid-flow models.[35] This coupled model considers growth and dissolution as a function of thermal excursions experienced by the inclusions due to fluid flow in the weld metal. All of these inclusion models were tested for gas-shielded welding processes (*e.g.*, gas–metal arc welding), slag-shielded welding processes (*e.g.*, shielded metal arc and submerged arc welding), and, to a limited extent, on the high-energy-density welding processes (*e.g.*

electron beam and laser welding). In an attempt to extend the inclusion model to a wide range of welding processes, current research has focused on inclusion formation in self-shielded flux-cored arc-welding processes (FCAW-S).[36]

During the FCAW-S process, there is no shielding by either gas or slag. Because there is no intentional shielding, oxygen and nitrogen from the atmosphere may dissolve into the liquid weld metal and produce porosity. To alleviate this problem, tubular electrodes containing Al, Ti, and Zr were used.[37,38] These elements react with dissolved oxygen and nitrogen to form oxides and nitrides, respectively. The tendencies to form these oxide and nitride inclusions were evaluated in two weld compositions produced by the FCAW-S process [see **Table 1**]. The inclusions in these welds were characterized with optical microscopy, scanning electron microscopy, and transmission electron microscopy. The types of inclusions were identified through composition measured by energy-dispersive spectroscopy.

The microstructural characterization showed that predominant inclusions in the weld "H" were aluminum nitrides [see **Figs. 2**(a) and 2(b)]. Detailed analyses of the extraction replica did not show the presence of Al_2O_3 or any other oxides or titanium carbonitride. Thermodynamic stability diagrams for the Fe–Al–O, Fe–Ti–N, and Fe–Al–N systems that consider the interaction with other alloying elements (including C and Mn) were calculated for 1 800 K using ThermoCalc® software.[39] The stability diagram for Weld H [see Fig 2(c)] shows that Al_2O_3 formation is not feasible. Even though there is a large concentration of aluminum in this weld, only AlN will form. This observation is in agreement with the experimental observation. Detailed analyses show that this outcome is due to the thermody-

Table 1. Composition of self-shielded flux-cored arc welds.

ID	C (wt.%)	Si (wt.%)	Mn (wt.%)	Al (wt.%)	Ti (wt. PPM)	O (wt. PPM)	N (wt. PPM)	Fe
H	0.23	0.28	0.50	1.70	30	60	640	Balance
L	0.15	0.30	0.64	0.53	580	300	330	Balance
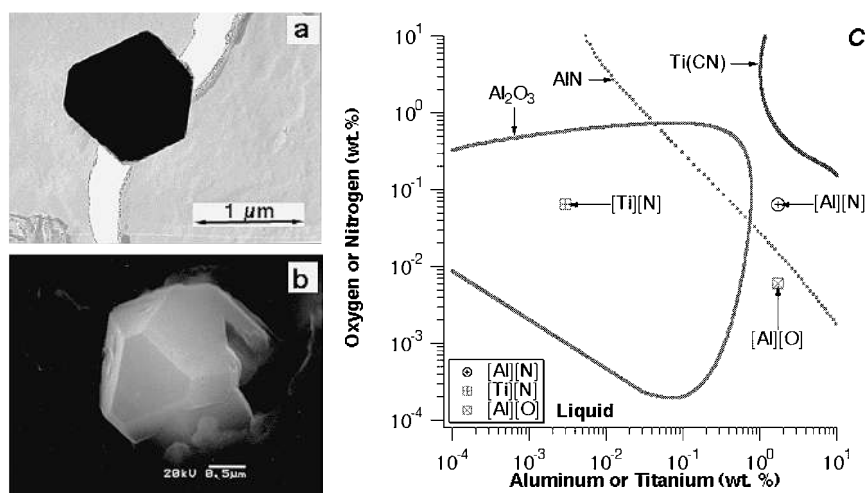
Fig. 2. (a) Transmission electron micrograph showing the presence of aluminum nitride inclusion in the "H" weld, (b) scanning electron microscopy image of similar inclusion, and (c) calculated stability diagram at 1 800 K for Fe–Al–O, Fe–Al–N and Fe–Ti–N for the base weld composition of steel H. The stability diagram shows that for this weld composition, the Al_2O_3 and Ti(CN) reaction will not occur and that the AlN reaction will be promoted.
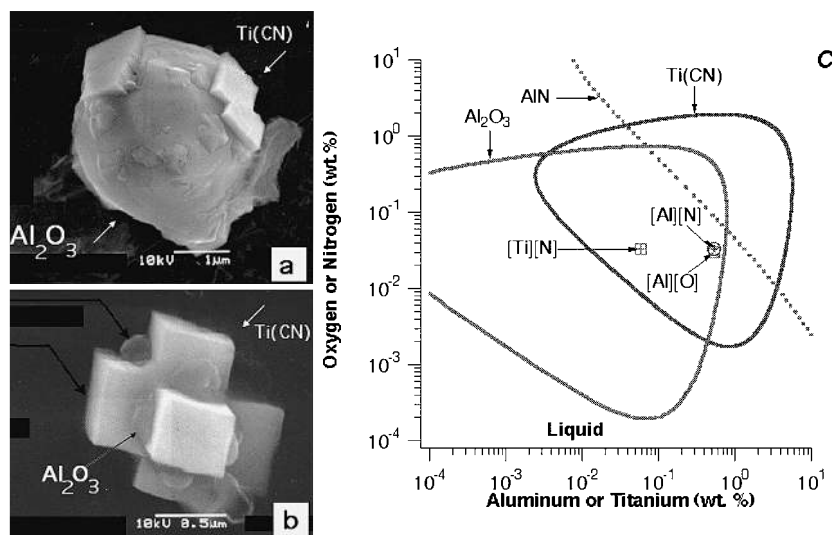
Fig. 3. (a) Scanning electron microscopy images showing (a) the heterogeneous nucleation of Ti(CN) on an Al_2O_3 inclusion, (b) an Al_2O_3 formation on a facetted Ti(CN) inclusion, and (c) a calculated stability diagram at 1 800 K for Fe–Al–O, Fe–Al–N and Fe–Ti–N for the base "L" weld composition. The stability diagram shows that for this steel composition, the Al_2O_3 and Ti(CN) reactions are promoted and that the AlN reaction is not feasible.

namic interaction between aluminum, oxygen, and nitrogen on the thermodynamic stability of liquid steel and Al_2O_3. The stability diagram for Weld H shows that the supersaturation of titanium and nitrogen is not sufficient to induce a Ti(CN) reaction.

The diagrams also show, in a counterintuitive way, that the reduction of aluminum concentration in this weld will lead to Al_2O_3 formation. The microstructural characterization of the "L" weld shows spherical Al_2O_3 oxide inclusions with heterogeneous nucleation of a facetted Ti(CN) phase on the surface [see **Fig. 3**(a)]. Other inclusions composed of highly facetted Ti(CN) with heterogeneous formation of Al_2O_3 on the facets. These observations indicate that both oxides and nitrides form simultaneously and that the inclusions tend to act as heterogeneous nucleation sites for other phases. Detailed analyses of extraction replicas from the weld did not show any presence of AlN inclusions. The calculated stability diagram for Fe–Al–N, Fe–Al–O and Fe–Ti–N for the "L" weld is shown in Fig. 3(c). The diagram shows that Al_2O_3 and Ti(CN) reaction is possible; however, AlN reaction is not feasible for the nominal composition at 1 800 K. This result is in agreement with the experimental observations.

The above results demonstrate that it is possible to describe inclusion formation in a wide range of welding processes by employing equilibrium thermodynamic calculations that consider multicomponent interactions in liquid steel.

3. Weld Solidification Microstructure

The effect of weld composition and cooling rate on the solidification grain structure, alloying element partitioning, and phase selection has been studied extensively.[40] The previous section illustrated that, depending upon aluminum concentration, either an aluminum oxide reaction or an aluminum nitride reaction can be triggered. This reaction may lead to different amounts of aluminum remaining in the so-

lution. In this study, the effect of aluminum concentration on the solidification microstructure was considered in self-shielded Fe–C–Al–Mn steel welds [see Table 1] through computational thermodynamic and kinetic calculations.

The microstructure of weld H contained columnar dendrites of δ-ferrite with classical α-ferrite microstructure between the dendrites [see **Fig. 4**(a)]. Thermodynamic calculations indicate following phase transformation sequence. (1) as the weld cools, first δ-ferrite forms from the liquid. (2) With further cooling, the austenite may nucleate at the interdendritic δ-ferrite regions and grow into the δ-ferrite. (3) As cooling continues below the solidus temperature, diffusion-controlled growth of austenite into δ-ferrite can occur. (4) The transformation of δ-ferrite to austenite may not reach completion due to extended stability of δ-ferrite. (5) At low temperatures (below 1 000 K), the austenite that formed at high temperature will decompose into the classical α-ferrite microstructure. This sequence is in general agreement with the experimentally observed microstructure. The kinetics of the transformation were evaluated with a diffusion-controlled growth model.[41,42] The solidification and subsequent solid-state transformation during cooling of the weld from 1 800 K at a rate of 10 K s^{-1} was simulated. The kinetic calculations [see Fig. 4(b)] reiterated that the retention of δ-ferrite is essentially due to incomplete austenite formation, as shown by the presence of >40% ferrite, at 1 500 K. Further cooling (below 1 500 K) did not change the amount of austenite greatly before the onset of low-temperature α-ferrite formation. Other calculations also show that increase in the weld-cooling rate would lead to retention of more δ-ferrite. This result was also in agreement with the experimental observations.[43]

Thermodynamic calculations of weld L indicate that even in this weld, δ ferrite would form from the liquid first. The calculations also show that the austenite that forms in the interdendritic regions is expected to replace the δ ferrite completely and would transform to the classical δ-ferrite microstructure. In agreement with these predictions, the
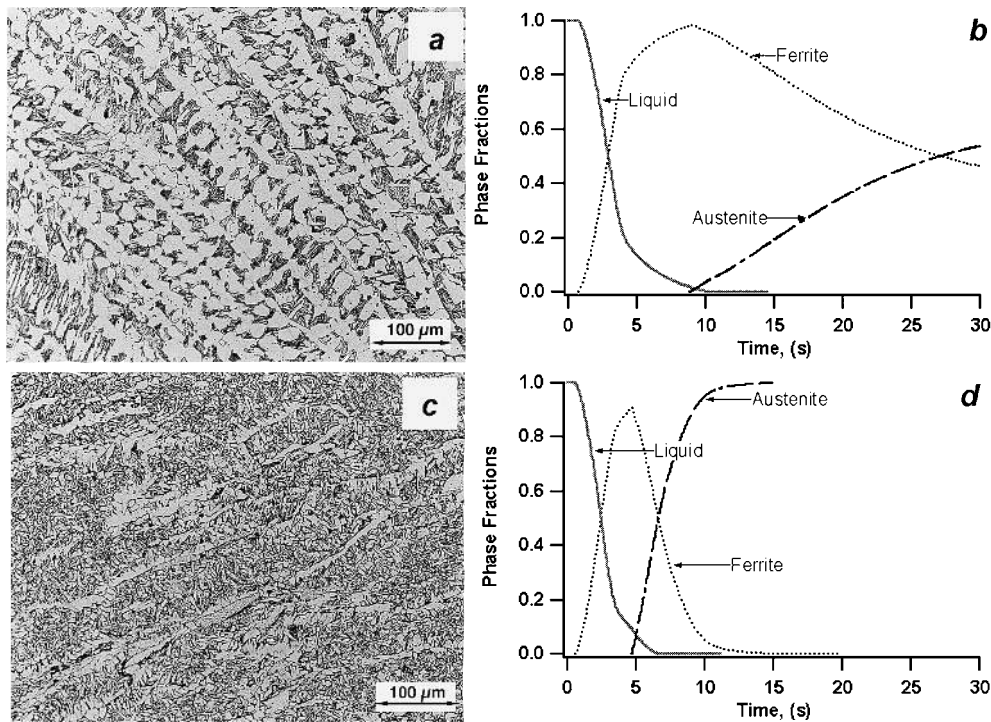
Fig. 4. (a) Optical microscopic view of columnar dendritic δ-ferrite microstructure in a weld with composition Fe–0.23wt%C–0.5wt%Mn–1.7wt%Al–30wtPPM T–60wtPPM O–640wtPPM N. (b) Calculated phase fraction for the same weld as a function of cooling time from 1 800 K at a rate of 10 K s^{-1} based on a diffusion-controlled growth model. (c) Optical microstructure of a weld with composition Fe–0.15wt%C–0.6wt%Mn–0.5wt%Al–580wtPPM Ti–300wtPPM O–330wtPPM N, showing classical α-ferrite microstructure that forms at temperatures below ~1 000 K from a 100% austenite phase. (d) Calculated phase fraction, based on the diffusion controlled growth model, for the same weld composition as a function of cooling time from 1 800 K at a rate of 10 K s^{-1}.

final microstructure [see Fig. 4(c)] contained a fine α-ferrite microstructure. The kinetics of austenite growth into δ-ferrite at high temperature were evaluated further with a kinetic model.[41,42] The calculations [see Fig. 4(d)] show that 100% austenite formed as the weld cooled to 1 600 K. The variation of cooling rate expected in the FCAW-S process was also evaluated. The results show that weld metal is expected to transform to 100% austenite for all cooling rates, therefore guaranteeing that a fine α-ferrite microstructure forms from the austenite. These results are in agreement with the experimental observations. These results show that the solidification and subsequent solid-state transformations at high-temperature can be predicted successfully with computational thermodynamic and kinetic calculations.

4. Rapidly Cooled Weld Microstructure

The results in the previous section assumed that solidification always occurs with δ-ferrite as the primary phase formation. This is based on the thermodynamic phase diagram. It did not consider the potential change in solidification mode at high-cooling-rates. Solidification may then occur with significant undercoolings below their equilibrium stability temperatures. Most relevant nonequilibrium solidification features in welding occur as a result of increased liquid-solid interface velocities under rapid cooling conditions. This increased velocity may lead to changes in solidification morphology, partitioning, and primary phase selections.[44–49] In welds, epitaxial solidification occurs from the heat-affected-zone, the nucleation of solid phase occurs readily.

To explore the possibility of primary solidification by a nonequilibrium phase in low-alloy steels, weld microstructure evolution in the H Weld [see **Table 1**] was investigated as a function of weld cooling rate using an *in situ* time-resolved X-ray diffraction (TRXRD) technique.[50] The welds were made by striking an arc on a stationary steel cylinder produced by a surface-cladding operation in which a self-shielded FCAW process was used. The gas–tungsten arc-welding process was used to produce stationary welds on these bars to remelt and resolidify the FCAW deposits. The average welding current was maintained at 110 A; voltage was maintained at 17.5 V. Two different welding conditions were used to vary the weld metal (WM) cooling rate. In the first experiment, the arc was extinguished at 17 s after initiation. This condition leads to a rapid cooling of the weld [see **Fig. 5**(a)]. During this experiment, the phase transformation events in both the HAZ and the WM were monitored. Previous research has shown that, during a static welding experiment, the measured peak cooling rates are six times higher (~1 500 K s^{-1}) than the normal weld-cooling rates (~250 K s^{-1}). In the second experiment, the arc current was reduced in a slope-down fashion from the peak current. This allowed the WM to cool slowly, as shown in Fig. 5(b). In this slow-cooling experiment, the transformation events were monitored only in the WM region of steel H. TRXRD measurements were performed on a 31-pole wiggler 10-2 beam line[51] at Stanford Synchrotron Radiation Laboratory with the Stanford Positron Electron Accumulation Ring. A photon energy of 12.0 keV ($\lambda=$
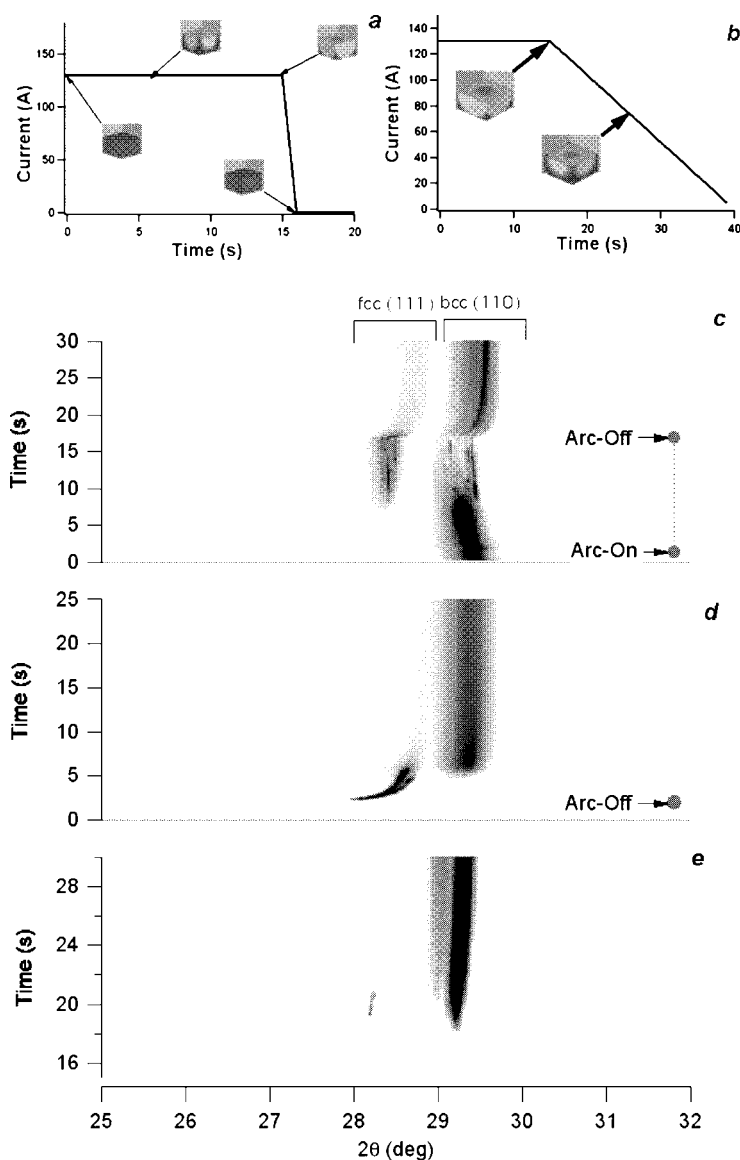
Fig. 5. Schematic illustration of gas tungsten arc spot weld experiment forcing (a) rapid weld cooling by sudden arc extinction and (b) slow weld cooling by gradual reduction of welding current. TRXRD data in an image format showing the fcc (111) and bcc (110) diffraction peaks from the (a) HAZ, (b) rapidly cooled WM region and (c) slowly cooled WM region.

0.1033 nm) was chosen to maximize the number of peaks diffracting into the 2θ window of the X-ray detector. In general, three body-centered cubic (bcc) ferrite peaks [(110), (200), and (211)] and three face-centered cubic (fcc) austenite peaks [(111), (200), and (220)] were identified. A 730-μm-diameter pinhole was used to achieve the time resolution necessary to capture phase transformations during the rapid thermal cycling. This setup yielded a beam flux on the sample of 10^{10} to 10^{11} photons/s. The diffraction spectra were collected at 0.05 s time intervals during transient heating and cooling of stationary arc welds.

The TRXRD data from the HAZ region are presented in Fig. 5(c). The measurements were made in the HAZ very close to the fusion line, where the HAZ temperatures were the highest. The results show the phase transformation events from the arc-on to the arc-off period. At room temperature, only diffraction peaks from the ferrite phase were observed. After the arc was struck, heating occurred and caused a shift in the ferrite bcc (110) peak to lower 2θ val-

ues as the crystal lattice of the ferrite phase expanded. After 7 s of arc-on, diffraction from austenite [fcc (111) peak] was observed. Continued weld heating led to an increase in austenite intensity. After the arc was shut off (17 s), the austenite rapidly transformed to ferrite, as shown by the decrease in austenite fcc (111) diffraction intensity and a corresponding increase in ferrite bcc (110) peak intensity. The persistence of ferrite at high temperature is evident from the intensity of bcc (110) diffraction peaks. This finding suggests that both ferrite and austenite are present near the fusion line.

The TRXRD data from WM region is presented in Fig. 5(d). While the arc was on, liquid was the only phase that was stable, as indicated by the absence of diffraction peaks. After the arc was extinguished, the liquid continued to exist as the only phase for an additional 0.2 s before the appearance of the austenite phase, as indicated by the fcc (111) peak. As the weld cooled further, the austenite peaks shifted toward higher 2θ values, indicating a decrease in lattice

spacing due to a drop in temperature. At about 3 s after the onset of solidification, ferrite was observed to coexist with the austenite, as indicated by the addition of the bcc (110) peak. Upon further cooling, the ferrite peaks also shifted toward higher 2θ values as the temperature approached ambient conditions. This result of primary austenite solidification was verified through repeated experiments. The *in situ* TRXRD results clearly show that, under rapid weld-cooling conditions, the equilibrium ferrite mode of solidification is replaced by nonequilibrium austenite.

To evaluate the hypothesis that the mode change was brought about by an increase in the cooling rate, weld current slope-down experiments were performed on steel H. The TRXRD measurements were obtained from the WM region of steel H during the slow- cooling experiment [see Fig. 5(e)]. The data show that at ~15 s after the slope down started, only liquid was present and no diffraction from ferrite or austenite was evident. The continued decrease in the welding current led to the appearance of bcc (110) diffraction peaks as the first solid phase. This confirmed the hypothesis that the reduced cooling rate would lead to primary ferrite solidification.

It is well known that the stability of the liquid-solid interface leads to different solidification phases and morphologies, and that it is indeed possible to describe these variations in primary phase solidification with an interface-response function model. Fukumoto and Kurz extended the binary model for dendrite solidification to the multicomponent Fe–Cr–Ni–C system by coupling the calculations with computational thermodynamics.[52–54] We have adopted the same approach here and have applied it to the Fe–C–Al–Mn system. The results [see **Fig. 6**(a)] show that the dendrite tip temperature of ferrite is higher than that that of the austenite for the entire range of interface velocities. This suggests that the ferrite interface will be far ahead of the austenite interface. Consequently, the predicted primary solidification phase will be ferrite. The plot also shows the calculated interface velocity for the spot-welding conditions.[55] The calculated variation in the partitioning coefficients for aluminum and carbon is shown in Fig. 6(b). The partitioning coefficients for Al and C for the austenite solidification mode are less than unity and tend to approach unity at higher liquid-solid interface velocities. In the case of ferrite solidification, carbon partitioning is similar to that of austenite. However, the partitioning coefficient for aluminum is greater than unity and tends to approach unity at higher velocities. The quantitative results from interface function models for the steel H do not in themselves support the observed transition from equilibrium ferrite to nonequilibrium austenite solidification. The calculations essentially show that the primary ferrite solidification would occur for all interface velocities. Even though this result is in agreement with slow-cooling-rate welds [see Fig. 5(d)], it is not in agreement with results from rapidly cooled welds [see Fig. 5(c)]. Further work is needed to understand this inconsistency.

5. Competition between Bainite and Acicular Ferrite Formation

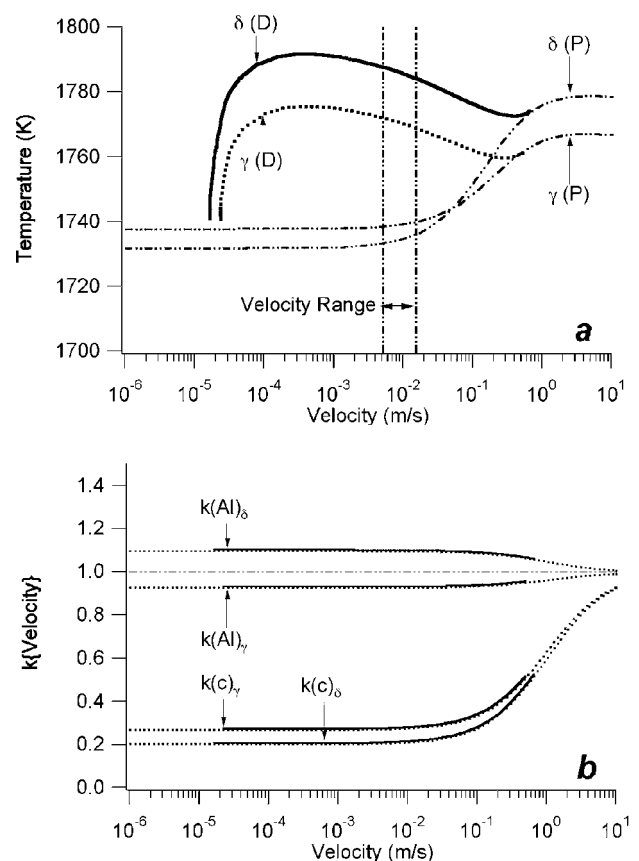The transformation of austenite to various ferrite mor-

Fig. 6. (a) Calculated dendrite tip temperature and planar interface temperature for ferrite and austenite solidification for a steel composition Fe–0.23wt%C–0.5wt%Mn–1.7wt%Al as a function of liquid-solid interface velocity. (b) Corresponding variation in partition coefficient for aluminum and carbon (dotted potion is for planar growth and solid line for dendritic growth).

phologies, including allotriomorphic-, Widmanstätten-, bainitic- and acicular-ferrite in steel welds has been studied extensively.[7–10,14,56,57] However, there is a need to develop models to describe the competition between the acicular ferrite and bainite reactions. The bainite and acicular ferrite form by similar transformation mechanisms except for the nucleation sites.[58] Bainite nucleates along the austenite–austenite grain boundary or along the ferrite–austenite grain boundary. In contrast, acicular ferrite nucleates intragranularly on inclusions within the austenite grains.[56,59] Based on energetic considerations, the heterogeneous nucleation of ferrite on inclusions may be less favorable than nucleation on the boundaries.[60–62] Therefore, as long as the free boundaries exist, the bainitic transformation kinetics will be more rapid than the transformation kinetics for acicular ferrite. Previous research has shown that it is possible to reduce the nucleation rate of bainite along the austenite grain boundaries by forming allotriomorphic ferrite all along the austenite grain boundary, thereby promoting acicular ferrite formation.[59] Kinetics of both acicular ferrite and bainite transformations are affected by autocatalysis; *i.e.*, previously formed ferrite subunits initiating the nucleation of other ferrite subunits. In this section, some of the preliminary work on modeling the relative competition between acicular ferrite and bainite is presented.

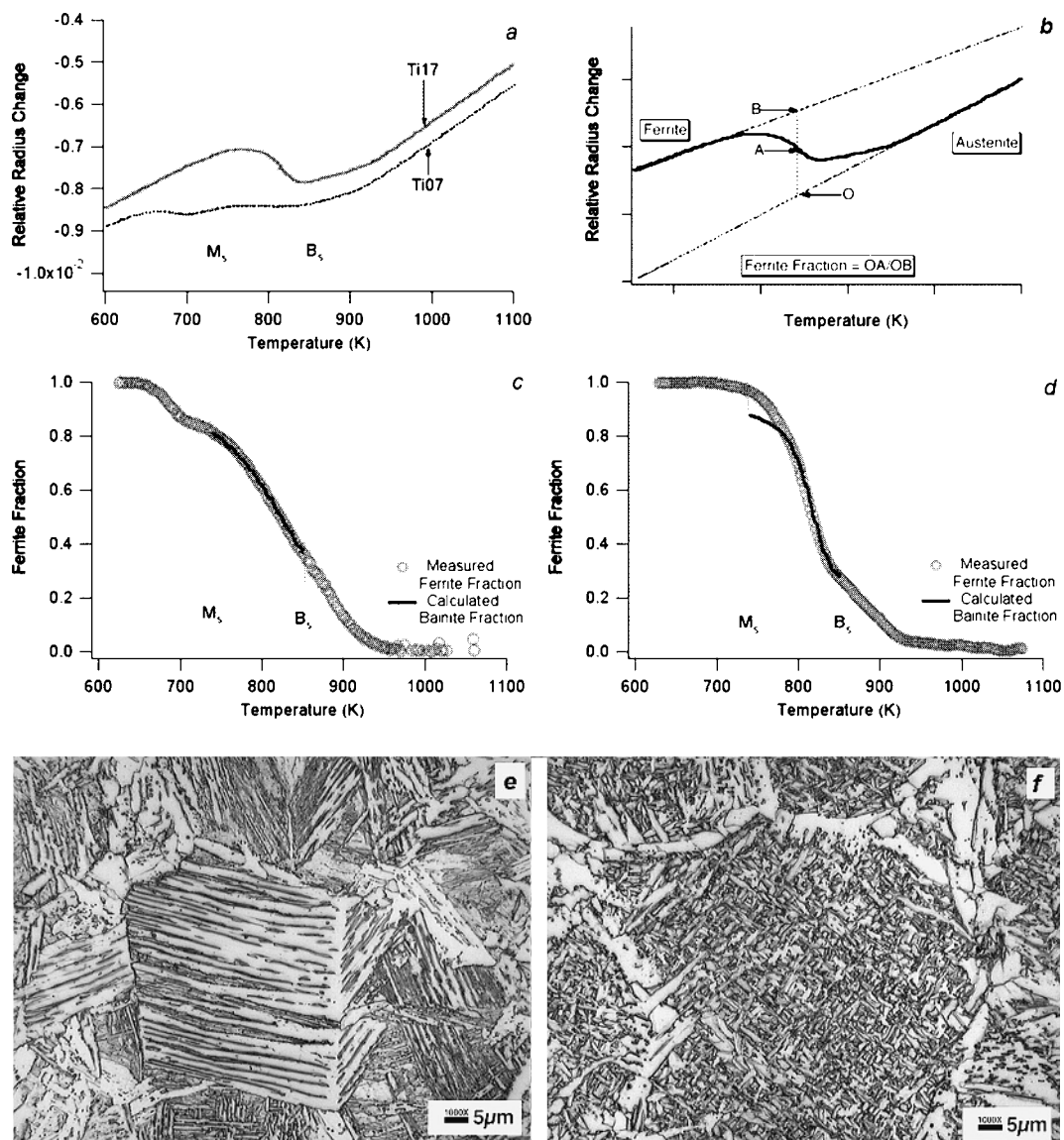Controlled thermal cycle experiments were performed on

low-alloy steel welds with two different titanium levels (7 and 17 wt. PPM). Only MnO·SiO$_2$ inclusions were found in the welds containing 7 wt. PPM Ti (Ti07). These welds have a predominantly bainitic microstructure in the WM region because MnO·SiO$_2$ does not take part in nucleating acicular ferrite. In contrast, Ti-rich oxides were found on the surfaces of MnO·SiO$_2$ inclusions in welds containing 17 wt. PPM Ti (Ti17). These welds have a predominantly

acicular ferrite microstructure. Both types of welds have similar hardenability, as indicated by the nominal composition (see **Table 2**). Rods of 6.35 mm diameter were machined from all-WM test specimens. The samples were austenitized at 1 200°C for 10 min and were cooled at a rate of 50 K s^{-1}. This cooling rate was designed so that a thin allotriomorphic ferrite layer would form along the austenite grain boundaries before the onset of bainitic/acicular ferrite formation.

The measured relative radius changes for both the samples are shown in **Fig. 7**(a). The plots indicate that the transformation kinetics are sluggish in the Ti07 weld compared with those of the Ti17 weld. A geometrical method [see Fig. 7(b)] developed by Eldis[63] was used to convert the measured transformation strains into a volume fraction. The converted ferrite fraction is shown as a function of temperature in Figs. 7(c) and 7(d). The data from the Ti07 welds

Table 2. Composition of Ti-containing low-alloy steel weld metals.

Sample ID	C (wt.%)	Si (wt.%)	Mn (wt.%)	Ti (wt.PPM)	O (wt.PPM)	N (wt.PPM)	Fe
Ti07	0.08	0.3	16	7	360	6	Balance
Ti17	0.08	0.3	1.6	17	350	6	Balance

Fig. 7. (a) Measured relative radius change from Ti07 and Ti17 welds (the data have been offset in the *y* axis for clarity) as a function of temperature while cooling from 1 473 K at a rate of 50 K s^{-1}. (b) Methodology to convert the relative length change to ferrite fraction. Measured ferrite fraction as a function of temperature for (c) Ti07 and (d) Ti17 weld as a function of temperature. The plots in (c) and (d) also show the calculated bainite fraction using a published kinetic model for bainitic transformation. Optical micrographs of (e) Ti07 sample with predominantly bainitic and (f) Ti17 sample containing predominantly acicular ferrite microstructure, after the simulated weld thermal cycle experiment.

showed a change in transformation rate at $\sim 700\,K$, which is below the calculated martensite start (Ms) temperature. This change is interpreted as evidence of martensite formation. The results suggest that the Ti07 welds might have a mixture of bainite and martensite. The plots indicate that the transformation kinetics just below the bainitic start (B_s) temperature for Ti17 welds are slightly more sluggish than the kinetics for Ti07. Interestingly, the rate of transformation for Ti17 welds increased above that of the Ti07 welds after certain undercooling below Bs temperature.

The corresponding microstructures of the Ti07 and Ti17 samples are shown in Figs. 7(e) and 7(f). The Ti07 samples clearly show predominantly bainitic microstructure, and the Ti17 samples clearly showed predominantly acicular ferrite microstructure. These results were interpreted based on bainite transformation kinetic theory.[64–67]

According to this published bainite transformation kinetic theory,[64–67] the growth of bainite occurs by subsequent formation of a ferrite subunit by a diffusionless mechanism. Additionally, the carbon partitioning from this plate occurs after the cessation of growth. As a result, further nucleation of the subunit will take place from an austenite that is enriched in carbon. This leads to cessation of bainite formation when the carbon content of the austenite reaches T_0 composition (or T_0' with $400\,J\,mol^{-1}$ strain energy). In addition, the model also allows for enhancement of the nucleation through the autocatalysis effect due to previous ferrite subunits. With this model, the rate of change in extent of the transformation at a temperature for bainite formation is given by the following equation,[67]

$$\frac{d\xi}{dt} = \left(\frac{uK_1}{\theta}\right)(1-\xi)(1+\beta\theta\xi)$$

$$\times \exp\left\{\left[\frac{K_2}{RT}\left(1+\frac{\Delta G_m^0}{r}\right)\right] + \left[\frac{K_2(\Delta G_m^0 - G_N)}{rRT}\xi\right]\right\} \quad ....(1)$$

where

K_1 is a parameter related to austenite grain boundary surface area per unit volume,
u is the ferrite subunit volume,
ξ is the current extent of transformation,
θ is the maximum bainite volume fraction that can form at that temperature,
K_2 is a constant,
R is gas constant,
T is temperature in Kelvin,
ΔG_m^0 is the maximum driving force of the nucleation of ferrite,
r is another constant given by $2\,540\,J\,mol^{-1}$,
G_N is the Universal nucleation function given by G_N $(J\,mol^{-1}) = 3.6375T_C - r$,
β is the autocatalysis factor.
The autocatalysis factor is given by the following equation,

$$\beta = \lambda_1(1 - \lambda_2\bar{x}) \quad ....(2)$$

where $\bar{x}$ is the bulk carbon concentration in the units of mole fraction λ_1 and λ_2 and are constants. Previous re-

Table 3. Best-fit coefficients for a bainite kinetic model derived with the transformation data from Ti07 and Ti17 samples.

Microstructure	K_1	λ_i
Bainite	1.0×10^{17}	4
Acicular ferrite	4.4×10^{16}	34

searchers using isothermal kinetic data derived the constants K_1, K_2, and λ_2[67] and the variation of subunit volume with temperature. The K_1 parameter represents the nucleation rate of bainite at any boundary. If the austenite grain boundaries are free, K_1 for bainite formation will be related to grain boundary area per unit volume ($S_V^{\gamma-\gamma}$).[65] If the austenite grain boundaries are decorated by the allotriomorphic ferrite, it will be related to the allotriomorphic ferrite–austenite interfacial area per unit volume ($S_V^{\gamma-\alpha}$) that is capable of nucleating.[68] In the case of acicular ferrite, the K_1 parameter is related to the inclusion-austenite interfacial area ($S_V^{\gamma-inc}$) that is capable of nucleating bainitic subunits.[19,24,25]

The additivity law was assumed, and Eq. (1) was applied to the transformation data shown in Fig. 7 in the temperature range between the B_s and M_s temperatures. The best-fit parameters were obtained [see **Table 3**] assuming $2.098\times10^4\,J\,mol^{-1}$ as a value for K_2 of and 30.327 as a value for λ_2. The ΔG_m^0 is calculated assuming praequilibrium transformation using methodology described in the published literature[69] and online software repository.[†] The Table 3 shows that the K_1 and λ_1 values for Ti07 welds were different from the values for the Ti17 welds. The variation of ferrite fraction predicted using fitted values are shown in Figs. 7(c) and 7(d). The analysis assumes that only bainitic ferrite formed in Ti07 samples and that only acicular ferrite formed in Ti17 samples. Although this assumption is valid based on the microstructural observations, it may be complex in other conditions. Such situations may occur when the austenite grain boundaries are not fully decorated with allotriomorphic ferrite.[70] Detailed analysis of model predictions and experimental ferrite fractions from Figs. 7(c) and 7(d) show some interesting features. In the case of Ti07 welds, the maximum experimental ferrite fraction achieved at 737 K is 0.81, and the kinetic model was able to fit this value very well. In contrast, the maximum experimental ferrite fraction achieved at 737 K is 0.97, although the model predicts only 0.87. This result shows that the transformation to acicular ferrite appears to go further than bainitic transformation. This change may be related to larger carbon trapping between the acicular ferrite subunits than that between the bainitic ferrite subunits.[66] Additionally, the K_1 value for Ti07 welds was higher than the value for Ti17 welds, and the autocatalysis factor for Ti17 weld is higher than that for Ti07 welds. Recently, Tszeng[71] theorized that the effect of autocatalysis on bainitic transformation kinetics is based on the shape of the bainite subunit. In addition, theoretical consideration of changes in $S_V^{\gamma-\gamma}$, $S_V^{\gamma-\alpha}$, $S_V^{\gamma-inc}$ and K_1 on and the types of inclusion characteristics[24] on competition between acicular

---

[†] Materials Algorithms Project Program Library: http://www.msm.cam.ac.uk/map/steel/programs/mucg46-b.html
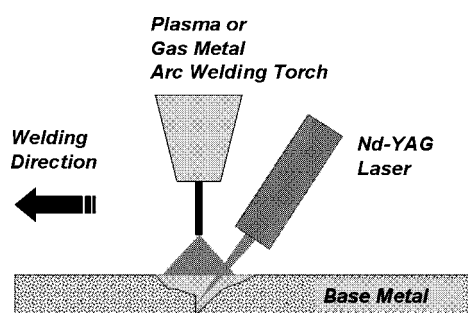
Fig. 8. Schematic illustration of laser-assisted arc-welding setup that combines the advantages of a low-heat input laser with the flexibility of changing the weld metal composition through consumable selection and shielding gases.

ferrite and bainitic ferrite for generic weld metal composition is being pursued further through theories of simultaneous transformation kinetic models.[72]

The above results indicate that microstructural control necessitates that the welding process must be capable of varying the dissolved gases (through gas shielding, slag shielding, or deoxidizer addition), rapid cooling rates and precise control of WM composition. Although, above control of the evolution of WM microstructure can be achieved with traditional welding processes (including shielded metal arc welding, submerged arc welding, flux-cored arc welding and gas–metal arc welding), the added constraint of reducing weld heat input for welding ultra fine-grained steel makes the application of the traditional processes difficult. The newly developed laser-assisted arc-welding (LAAW) process shows great potential. The LAAW process requires a minimum joint-fit setup, which makes it practical for a wide range of weld geometries. The laser heat source and arc heat source are coupled (see **Fig. 8**), and, and the heat-input to the welds can be minimized by controlling the arc power and laser power. In addition, shielding gas and filler metal can be used to precisely control inclusion characteristics and microstructure evolution. Currently, the LAAW process is being evaluated at ORNL for wide range of steels.[73]

6. Summary and Conclusions

The results presented in this paper have demonstrated that it is indeed possible to control the evolution of WM microstructure by modifying inclusion characteristics, WM solidification, and solid-state transformation. The competition between oxide and nitride inclusions in Fe–C–Al–Mn steel weld was described. The roles of WM composition and cooling rate on solidification and subsequent solid-state transformation in Fe–C–Al–Mn welds were described with diffusion-controlled-growth models. The formation of non-equilibrium austenite solidification at rapid cooling in Fe–C–Al–Mn stationary welds was successfully identified with an *in situ* TRXRD technique. This nonequilibrium phase selection was analyzed with interfacial response function models. Rapid transformations of austenite to acicular ferrite in steels with titanium-containing inclusions were compared with sluggish transformation of austenite to bainite during continuous cooling. Theoretical evaluation of these results showed that acicular ferrite formation has a large autocatalysis factor compared with that of bainite. The LAAW process was introduced as a potential process for welding ultra fine-grained steels.

REFERENCES

1) A. Belyakov, Y. Sakai, T. Hara, Y. Kimura, and K. Tsuzaki: *Scr. Mater.*, **45** (2001), 1213.
2) S. Takaki, K. Kawasaki, and Y. Kimura: *J. Mater. Process. Technol.*, **117** (2001), 359.
3) F. G. Caballero, H. K. D. H. Bhadeshia, K. J. A. Mawella, D. G. Jones and P. Brown: *Mater. Sci. Technol.*, **18** (2002), 279.
4) C. Ouchi: *ISIJ Int.*, **41** (2001), 542.
5) A. Ali and H. K. D. H. Bhadeshia: *Mater. Sci. Technol.*, **7** (1991), 895.
6) S. S. Babu: Ph. D. Thesis, University of Cambridge, UK, (1992).
7) R. E. Dolby: Proc. Int. Conf. on Advances in the Physical Metallurgy and Applications of Steel, The Metals Society, London, (1981), 111.
8) G. M. Evans and N. Bailey: Metallurgy of Basic Weld Metal, Abington Publishing, Cambridge, UK, (1997).
9) D. J. Abson and R. J. Pargeter: *Int. Met. Rev.*, **31** (1986), 141.
10) O. Grong and D. K. Matlock: *Int. Met. Rev.*, **31** (1986), 27.
11) Y. Ito and M. Nakanishi: *Sumitomo Search*, **15** (1976), 42.
12) S. Liu and D. Olson: *Weld. J.*, **65** (1986), 139s.
13) Z. Zhang and R. A. Farrar: *Mater. Sci. Technol.*, **12** (1996), 237.
14) G. Thewlis: *Mater. Sci. Technol.*, **10** (1994), 110.
15) G. Thewlis, J. A. Whiteman and D. J. Senogles: *Mater. Sci. Technol.*, **13** (1997), 257.
16) O. Grong, A. O. Kluken, H. K. Nylund, A. L. Dons and J. Hjelen: *Metall. Mater. Trans. A*, **26A** (1995), 525.
17) Y. Hori, K. Ichikawa, S. Ohkita, S. Funaki, and N. Yurioka: *Q. J. Jpn. Weld. Soc.*, **13** (1995), 500.
18) J. M. Gregg and H. K. D. H. Bhadeshia: *Metall. Mater. Trans. A*, **25A** (1994), 1603.
19) J. M. Gregg and H. K. D. H. Bhadeshia: *Acta Metall. Mater.*, **42** (1994), 3321.
20.) S. Zhang, N. Hattori, M. Enomoto and T. Tarui: *ISIJ Int.*, **36** (1996), 1301.
21) T. Lee, H. J. Kim, B. Y. Kang and S. K. Hwang: *ISIJ Int.*, **40** (2000), 1260.
22) S. Chatterjee and N. S. Mishra: *Steel Res.*, **65** (1994), 138.
23) F. Ishikawa, T. Takahashi and T. Ochi: Solid→Solid Phase Transformations, ed. by W. C. Johnson, J. M. Howe, D. E. Laughlin and W. A. Soffa, The Minerals, Metals and Materials Society, Warrendale, PA, (1994), 171.
24) J. Lee: *Acta Metall. Mater.*, **42** (1994), 3291.
25) I. Madriaga and I. Gutierrez: *Acta Mater.*, **47** (1999), 951.
26) I. Madriaga, J. L. Romero and I. Gutierrez: *Metall. Mater. Trans. A*, **29A** (1998), 1003.
27) S. S. Babu, S. A. David, J. M. Vitek, K. Mundra and T. DebRoy: *Mater. Sci. Technol.*, **11** (1995), 186.
28) S. S. Babu, S. A. David, J. M. Vitek, K. Mundra and T. DebRoy: *Sci. Technol. Weld. Joining*, **4** (1999), 276.
29) N. Bailey and R. J. Pargeter: The Influence of Flux Type on the Strength and Toughness of Submerged Arc Weld Metal, The Welding Institute, Abington, (1988), 33.
30) A. Kluken and O. Grong: *Metall. Trans. A*, **20** (1989), 1335.

31) H. K. D. H. Bhadeshia and L.-E. Svensson: Mathematical Modeling of Weld Phenomena, ed. by H. Cerjak and K. E. Easterling, The Institute of Materials, London, (1993), 109.

32) T. Koseki, S. Ohkita and N. Yurioka: *Sci. Technol. Weld. Joining*, **2** (1997), 65.

33) J. W. Christian: The Theory of Transformations in Metal and Alloys–Part I Equilibrium and General Kinetic Theory, 2nd Ed., Pergamon Press, Oxford, (1981), 525.

34) S. S. Babu, F. Reidenbach, S. A. David, Th. Bollinghaus and H. Hoffmeister: *Sci. Technol. Weld. Joining*, **4** (1999) 63.

35) T. Hong, T. DebRoy, S. S. Babu and S. A. David: *Metall. Trans. B.*, **31B** (2000) 161.

36) M. A. Quintana, J. McLane, S. S. Babu and S. A. David: *Weld. J.*, **80** (2001), 98s.

37) D. J. Kotecki and R. A. Moll: *Weld. J.*, **49** (1970), 157s.

38) D. J. Kotecki and R. A. Moll: *Weld. J.*, **51** (1972), 138s.

39) B. Sundman, B, Jansson and J. O. Andersson: *Calphad*, **9** (1985), 1.

40) S. A. David and J. M. Vitek: *Int. Met. Rev.*, **34** (1989), 213.

41) J.-O. Andersson, L. Hoglund, B. Jonsson and J. Ågren: Fundamentals and Applications of Ternary Diffusion, ed. by G. R. Purdy, Pergamon Press, New York, (1990), 153.

42) A. Engstrom, L. Hoglund and J. Agren: *Metall. Mater. Trans. A*, **25A** (1994). 1127.

43) S. S. Babu, S. A. David and M. A. Quintana: *Weld. J.*, **80** (2001), 91s.

44) M. J. Aziz: *J. Appl. Phys.*, **53** (1982), 1158.

45) W. Kurz, B. Giovanola and R. Trivedi: *Acta Metall.*, **34** (1986), 823.

46) N. Suutala: *Metall. Trans. A*, **14A** (1983), 191.

47) R. Trivedi and W. Kurz: *Int. Matter. Rev.*, **39** (1994), 49.

48) O. Hunziker, M. Vandyoussefi and W. Kurz: *Acta Mater.*, **46** (1998), 6325.

49) S. A. David, J. M. Vitek and T. L. Hebble: *Weld. J.*, **66** (1987), 289s.

50) S. S. Babu, J. W. Elmer, S. A. David and M. A. Quintana: *Proc. R. Soc. (London) A.*, **458** (2002), 811.

51) V. Karpenko, J. H. Kinney, S. Kulkarni, K. Neufel, C. Pope, K. G. Tirsell, J. Wong, J. Cernio, T. Troxel and J. Yang: *Rev. Sci. Instrum.*, **60** (1989), 1451.

52) S. Fukumoto and W. Kurz: *ISIJ Int.*, **37** (1997), 677.

53) S. Fukumoto and W. Kurz: *ISIJ Int.*, **38** (1998), 71.

54) S. Fukumoto and W. Kurz: *ISIJ Int.*, **39** (1999), 1270.

55) W. Zhang and T. DebRoy: unpublished research, The Pennsylvania State University, PA, (2002).

56) H. K. D. H. Bhadeshia: Bainite in Steels: Transformations, Microstructure, and Properties, 2nd Ed., The Institute of Materials, London, (2001).

57) H. K. D. H. Bhadeshia, L.-E. Svensson and B. Gretoft: *Acta Metall.*, **33** (1985), 1271.

58) G. I. Rees and H. K. D. H. Bhadeshia: *Mater. Sci. Technol.*, **10** (1994), 353.

59) S. S. Babu and H. K. D. H. Bhadeshia: *Mater. Sci. Technol.*, **6** (1990), 1005.

60) R. A. Ricks, G. S. Barrite and P. R. Howell: Proc. Conf. on Solid State Phase Transformations 87, The Institute of Metals, London, (1979), 463.

61) R. A. Ricks and G. S. Barrite: *J. Mater. Sci.*, **17** (1982), 732.

62) S. J. Jones and H. K. D. H. Bhadeshia: *Metall. Mater. Trans. A*, **28A** (1997), 2005.

63) G. T. Eldis: Hardenability Concepts with Applications to Steel, ed. D. V. Doane and J. S. Kirkaldy, American Institute of Mining, Metallurgical and Petroleum Engineer, Inc., Warrendale, PA, (1978), 126.

64) H. K. D. H. Bhadeshia: *J. de. Physique*, **43** (1982), C4-443.

65) G. I. Rees and H. K. D. H. Bhadeshia: *Mater. Sci. Technol.*, **8** (1992), 985.

66) G. I. Rees and H. K. D. H. Bhadeshia: *Mater. Sci. Technol.*, **8** (1992), 994.

67) N. A. Chester and H. K. D. H. Bhadeshia: *J. Phys. IV France*, **7** (1997), C5-41.

68) S. S. Babu and H. K. D. H. Bhadeshia: *Mater. Sci. Eng. A*, **A142** (1991), 209.

69) H. K. D. H. Bhadeshia: *Met. Sci.*, **15** (1981), 175.

70) S. S. Babu and H. K. D. H. Bhadeshia: *Mater. Trans. JIM*, **32** (1991), 679.

71) T. C. Tszeng: *Mater. Sci. Eng. A*, **A293** (2000), 185.

72) S. J. Jones and H. K. D. H. Bhadeshia: *Acta Mater.*, **45** (1997), 2911.

73) J. M. Vitek, S. A. David, M. W. Richey, J. Biffin, N. Blundell and C. J. Page: *Sci. Technol. Weld. Joining*, **6** (2001), 305.